Surface effects on Pt-Ni single crystals calculated with the embedded-atom method

H. Stadler, W. Hofer, M. Schmid, and P. Varga
Institut für Allgemeine Physik, Technische Universität Wien, A-1040 Wien, Austria
(Received 10 March 1993)

Recent scanning-tunneling-microscopy (STM) experiments on $Pt_{25}Ni_{75}(111)$ and $Pt_{10}Ni_{90}(110)$ surfaces showing lattice mismatch dislocations near the surface and surface ordering phenomena have been verified in simulation calculations using the embedded-atom method (EAM). It was found that the EAM can be successfully applied for the calculation of ordering effects and crystal defects such as dislocations using energy minimization routines and Monte Carlo calculations. By comparing experimental data and EAM results, it was possible to determine the depth of the dislocations and therefore the number of layers with Pt enrichment on the surface. For the (111) face exhibiting surface ordering phenomena, the calculated short-range order is in agreement with STM data where the two species could be clearly distinguished.

I. INTRODUCTION

Recent scanning-tunneling-microscopy (STM) experiments[1–3] have shown that lattice mismatch dislocations caused by preferential sputtering are present on a $Pt_{25}Ni_{75}(111)$ surface. They form a network of subsurface dislocations visible as ditches in the STM image. It was found that the density of these dislocations depends on the ion dose as well as on the annealing temperature. The sputter gas influences the amount of Pt enrichment in the surface layers, depending on the penetration depth of the projectiles. The smaller the size of these atoms, the larger is the penetration depth and therefore the number of Pt enriched layers. On the other hand, a higher annealing temperature enhances the diffusion process and therefore decreases the Pt composition obtained by preferential sputtering. On top of these effects, experiments agree on a pronounced segregation of Pt on this surface.[4–6]

Similar to the (111) surface, there also is Pt enrichment due to preferential sputtering on the (110) surface.[3] One therefore would expect similar effects on this face. However, in contrast to the six possible Burgers vectors parallel to a (111) surface forming either perfect or Shockley partial dislocations, there is just one Burgers vector parallel to the surface of a (110) face, i.e., the perfect dislocation $\frac{1}{2}[1\bar{1}0]$. Therefore the dislocation system on this surface is quite different from the one on the (111) surface, as observed by STM on a $Pt_{10}Ni_{90}(110)$ surface.[3] In contrast to the network of subsurface dislocations formed on the (111) surface, dislocation lines parallel to the [100] direction are formed on the (110) face. Similar to the dislocation system encountered on the (111) surface,[1,2] there are also areas where the dislocations reach the surface. Here the associated Burgers vector could be unambiguously determined as $\frac{1}{2}[1\bar{1}0]$.

Other striking results[7] show that under certain tip conditions a distinction of the elements on a $Pt_{25}Ni_{75}(111)$ surface was possible. Thereby, surface chemical short-range ordering could be observed. This type of ordering phenomena has not been detected before, since the ordering is only local and therefore could not be detected by previous low energy electron diffraction measurements.

For comparison of these STM data and for obtaining information about the atomic arrangement and composition in deeper layers we have performed computer simulations using the embedded-atom method[8,9] for our calculations, a theory which has been developed by Baskes and Daw. Foiles[10] has applied the embedded-atom method (EAM) to the calculation of surface segregation and other surface-related phenomena. In the past years, the EAM has been applied to the calculation of many different physical properties such as segregation phenomena,[11–14] surface relaxation,[15,16] reconstructions,[17] and other structural data[18] with great success. Its ease of use and computational simplicity make it an excellent method for the calculation of surface properties. With the EAM, ensembles consisting of thousands of atoms can be easily calculated. This is a great advantage over *ab initio* calculations, where the number of atoms in the configuration is restricted to a couple of hundred atoms or less. Since the configurations for our calculations consisted of 4000–8000 atoms, *ab initio* calculations are ruled out with the computer systems available today.

In Sec. II we give an overview of the EAM and its application in energy minimization and Monte Carlo calculations. Section III deals with the application of this method for the verification of STM results showing lattice mismatch dislocations caused by preferential sputtering of $Pt_{25}Ni_{75}(111)$ and $Pt_{10}Ni_{90}(110)$ surfaces.[1–3] Finally, in Sec. IV we simulate the formation of surface ordering due to Pt enrichment on the surface.[7]

II. EMBEDDED-ATOM METHOD

A. Theory

As an application of density functional theory, the embedded-atom method[8,9] is used for the calculation of

the total energy of an arbitrary arrangement of atoms. The total energy is the summation of the individual contributions to the energy of all atoms in the ensemble. The energy contribution of each atom consists of two parts: the first one is the energy to embed an atom in a homogeneous electron gas with electron density ρ_h due to the surrounding atoms, the second term is a pair potential accounting for the core-core repulsion of two atoms. Therefore, the total energy $E_{\rm tot}$ can be written in the following way[9] (atomic units are employed throughout this paper):

$$E_{\rm tot} = \sum_i F_i(\rho_{h,i}) + \frac{1}{2}\sum_{\substack{i,j \\ i\neq j}} \Phi_{ij}(R_{ij}), \tag{1}$$

where F_i is the embedding energy for atom i due to the electron density $\rho_{h,i}$ of the surrounding atoms j. The sum over all atoms i of the ensemble leads to the embedding part of the total energy. The second term in Eq. (1) is the pair potential $\Phi_{ij}(R_{ij})$ which accounts for the core-core repulsion of two atoms i and j separated by the distance R_{ij}. The sum is over all pairs (i,j) of atoms in the ensemble and the factor $\frac{1}{2}$ accounts for counting all pairs twice. The host density $\rho_{h,i}$ can be closely approximated by summarizing the individual electron densities of the neighboring atoms ρ^a, i.e., $\rho_{h,i} = \sum_{j\neq i} \rho^a_j(R_{ij})$. The individual electron densities of each atom i, ρ^a, can be obtained from Hartree-Fock calculations.[19,20] Because these calculations do not account for the proper mixing of electronic configurations in the solid (e.g., $3d^8 4s^2$, $3d^9 4s^1$, or $3d^{10}$ for Ni), empirical parameters n_s and n_d have been defined, corresponding to the s-like and d-like content of the atomic density. The sum $n_s + n_d$ is fixed to be 10 for Ni and Pt. Therefore, the electron density ρ^a can be written as

$$\rho^a(R) = n_s\rho_s(R) + n_d\rho_d(R). \tag{2}$$

Both the embedding function $F(\rho)$ and pair potential $\Phi(R)$ must be determined by a fitting process described below.

The way $\rho_{h,i}$ is defined here proved successful in our calculations. We also tried analytical functions of the form $\rho(R) = DR^\beta(e^{-|\alpha|R} + 2^{(3+\beta)}e^{-2|\alpha|R})$ which have been successfully employed in some calculations,[21] where D, α, and β are parameters used to adjust the function to the form of ρ^a obtained from Hartree-Fock calculations. However, the results obtained with these analytical functions were very unstable so that particular Pt concentrations often could not be adjusted. Additionally, these functions did not exhibit the formation of a tetragonal $L1_0$ phase near 50% Pt, as can be derived from phase diagrams.[22,23] For these reasons we used the more complex functions obtained from Hartree-Fock calculations.

B. Fitting of the functions $F(\rho)$ and $\Phi(R)$

Determining proper embedding functions is the basis for obtaining good results. Care has to be taken in choosing appropriate starting values for the various parameters to be fitted. We used the approach and the parameters described by Foiles, Baskes, and Daw,[15] which turned out to give proper embedding functions so that different calculated properties of the elements as well as alloy parameters are in good agreement with experimental values. In this approach, Eq. (1) is compared with the Rose function,[24]

$$E(a) = -E_{\rm sub}(1 + a^*)e^{-a^*}. \tag{3}$$

This function reflects the change in energy with deviation of the lattice constant a from its equilibrium value, therefore reflecting the change in energy for the crystal under stress and strain. $E_{\rm sub}$ is the absolute value of the sublimation energy and a^* is a measure of the deviation from the equilibrium lattice constant,

$$a^* = (a/a_0 - 1)/(E_{\rm sub}/9B\Omega)^{1/2}. \tag{4}$$

In this expression, B is the bulk modulus, a is the lattice constant to be varied, a_0 the equilibrium lattice constant, and Ω the equilibrium volume per atom. The Rose function has been shown to be universal for a great variety of metals for both expansion and compression.[24]

Φ_{ij} is defined as the repulsive potential of the effective charges $Z(R)$,

$$\Phi_{ij} = Z_i(R)Z_j(R)/R, \tag{5}$$

where the subscripts i and j refer to the elements of the alloy. Foiles, Baskes, and Daw[15] have used the following function for $Z(R)$:

$$Z(R) = Z_0(1 + \beta R^\nu)e^{-\alpha R}. \tag{6}$$

Z_0 is taken to be the number of outer electrons of the atom. The parameters α and β and n_s from Eq. (2) have to be determined by means of a least square fitting process; ν was found to give best results when set to 1.

In the fitting process, the parameters are adjusted so as to give the best results for the elastic constants and vacancy formation energy of the pure elements as well as the dilute limits of the heats of solution of the binary alloy. From this fitting procedure, the functions $F(\rho)$, $Z(R)$, and $\rho(R)$ are obtained for both Pt and Ni.

Since the contribution to the total energy of each atom is a combination of embedding function and pair potential, a linear change in the embedding function can be compensated for by a change in the pair potentials, i.e.,

$$F_i(\rho) \to F_i(\rho) + a_i\rho,$$
$$\Phi_{ij}(R) \to \Phi_{ij}(R) - a_i\rho^a_j(R) + a_j\rho^a_i(R).$$

Therefore, the form of the pair potential functions is not exactly determined and not restricted to the one used in Eq. (5). Some authors[21] have used Morse potentials of the form $\Phi(R) = D(e^{-2\alpha(R-R_0)} - 2e^{-\alpha(R-R_0)})$, where the parameters D, α, and R_0 determine the exact form of the potential. Unfortunately these functions turned out to produce unstable results similar to those mentioned previously, so we used the form of the functions in Eqs. (5) and (6).

The validity of the functions was tested by calculating different properties of the pure elements and the alloys like vacancy-formation energy, vacancy-formation volume, surface energies, alloy heats of solution, and relaxation. Since we used the functions described by Foiles, Baskes, and Daw, our calculated values match exactly with the values given in Ref. 15.

C. Energy minimization calculations

Our calculations on dislocation phenomena were performed by means of energy minimization. Periodic boundary conditions were applied to minimize the number of atoms necessary for the calculations. We used a conjugate gradient algorithm[25] where the force gradient for each atom in the ensemble was calculated and the atomic coordinates were adjusted so as to move downhill on the potential energy surface, finally leading to a configuration with minimal potential energy.

Starting from the initial configuration, each atom is moved in the direction determined by its force gradient by a random displacement. Then the potential energy and force gradients of the new configuration are calculated and the ensemble is rearranged accordingly. This procedure is repeated until convergence is attained.

D. Monte Carlo calculations

The calculations of surface short-range ordering effects were done using Monte Carlo simulations, since this method is computationally simple and allowed us to obtain quick results. In contrast to the energy minimization calculations in Sec. II C, where the results depend on the initial configuration, the starting configuration has hardly any influence on the result in this approach since the configuration is changed with every Monte Carlo step. Each of these steps consists of two parts: first, an atom of the ensemble is picked and moved from its current position by a small random deviation, therefore accounting for thermal vibrations and allowing the system to relax. Additionally, the chemical identity of the atom is changed with a certain probability, allowing the system to change its chemical composition. After performing a large number of these steps (10^4–10^5 per atom), equilibrium is reached.

The simulations were performed using statistical mechanics with a grand canonical ensemble. In this approach the temperature, total number of atoms, and the relative chemical potentials are fixed. The probability of accepting a Monte Carlo step of the type described above (converting an A atom into a B atom) is given by[11]

$$P_{A\to B} = \frac{\Lambda_A^3}{\Lambda_B^3} e^{-(\Delta E+\mu_A-\mu_B)/k_BT}. \quad (7)$$

In this expression, Λ_A and Λ_B are the thermal de-Broglie wavelengths[26] of species A and B, ΔE is the energy difference of the two configurations, and μ_A and μ_B are the chemical potentials of the respective atoms. k_B is the Boltzmann constant and T is the temperature. Λ_A and Λ_B were fixed in our calculations.

In principle, two types of calculations have to be performed: first, bulk calculations for adjusting the chemical potentials to obtain the desired concentration of species A and B have to be done. For this reason different runs with varying differences $\mu_A - \mu_B$ of the chemical potential have to be made until the desired bulk concentration is obtained. For these calculations periodic boundary conditions have been applied in all three directions to exclude surface effects.

After the correct values of the chemical potentials have been obtained, a slab geometry is formed by removing the periodic boundary condition in the direction perpendicular to the desired surface. The slab should be sufficiently thick so that bulk conditions exist in the inner layers. This approach incorporates surface effects in the calculations and therefore is well suited for the types of calculations we performed.

After a sufficient number of Monte Carlo steps has been performed, equilibrium is reached and a file with the configurational data (types and positions of all atoms) is generated for data analysis.

III. CALCULATION OF DISLOCATION SYSTEMS

As mentioned in Sec. II C, energy minimization calculations were performed using embedding functions developed by Foiles, Baskes, and Daw.[15]

Typical dislocation spacings are ≈10–20 nm, the elementary cell of a hexagonal dislocation system as in Refs. 1 and 2 therefore covers an area of ≈100–400 nm^2. For the simulations, the slab should be about 30 layers thick. This would produce simulation configurations of roughly 50 000–200 000 atoms, leading to exceedingly long calculation times. We therefore restricted our simulations to crystals containing a couple of thousand atoms, representing sections through actual dislocation systems only.

A. Perfect dislocations on a $Pt_{25}Ni_{75}(111)$ surface

The term "perfect dislocation" refers to these types of dislocations that can be described by the possible lattice vectors which are smallest in magnitude. For the fcc structure, these dislocations are characterized by a Burgers vector of type $\frac{1}{2}\langle 110\rangle$.

For the simulations we used a configuration with a surface area 10.3 nm × 1.3 nm in size (240 atoms/layer), and a thickness of 6.1 nm (30 layers). The longer axis on the surface was taken to be the $[1\bar{1}0]$ direction which is parallel to the Burgers vector and perpendicular to the dislocation line. Periodic boundary conditions were applied in the $[1\bar{1}0]$ and $[\bar{1}\bar{1}2]$ directions to form a slab geometry. The configuration resulting from the application of periodic boundary conditions therefore exhibits parallel dislocation lines 10.3 nm apart, matching the value of ≈10 nm for the dislocation line spacing derived from STM images.

To account for the sputter-induced Pt enrichment at the surface, we used a concentration profile with three different Pt-Ni compositions, labeled "A," "B," and "C" in Fig. 1(a). Region "A" had the highest Pt concen-

tration and region "C" the lowest, this one taken to be the bulk concentration. This stepwise variation of the concentration is a rough approximation of the sputter-induced Pt enrichment. This effect is much more pronounced than segregation effects,[2] so segregation phenomena were neglected in our calculations. The Pt concentration for region "A" was 40% Pt, 35% for region "B," and 25% for region "C" (bulk). For simplicity, the atoms were distributed randomly in the layers, although bulk $Pt_{25}Ni_{75}$ can form an $L1_2$ phase[23] and the surface exhibits short-range ordering (see Sec. IV). Next, two neighboring $(1\bar{1}0)$ planes have been removed in regions

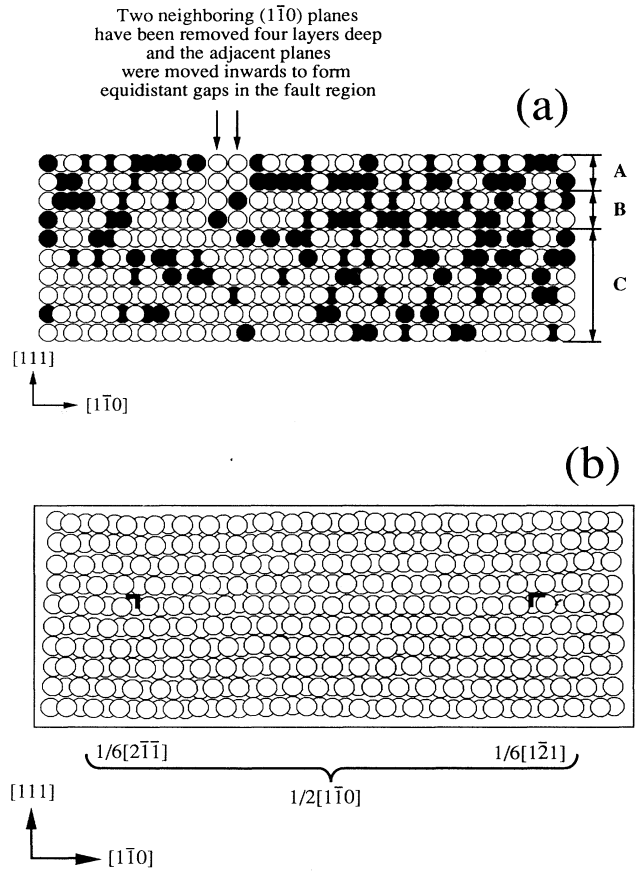

FIG. 1. Side view of a crystal before (a) and after (b) the calculation of lattice relaxation in the vicinity of a lattice mismatch dislocation (only the region in the vicinity of the dislocation core is shown). (a) shows the input configuration used for the calculations. The concentrations differ in regions "A," "B," and "C." In this figure, region "A" has 40% Pt, region "B" 35% Pt, and region "C" (the bulk) 25% Pt. Two neighboring atomic planes parallel to $(1\bar{1}0)$ have been removed in regions "A" and "B" (four layers deep) and the adjacent planes were moved inwards. Dark circles represent Pt atoms, light ones Ni. (b) Result of the calculations using configuration (a) as input. It was found that the $[1\bar{1}0]$ perfect dislocation splits up in two Shockley partials. To improve the clearness of the viewgraph, no distinction between atomic species has been made. The two inverted "L" symbols represent the dislocation cores whose Burgers vectors are indicated below.

"A" and "B" and the adjacent planes were moved inwards to form equidistant gaps in the region where the atoms have been removed. This process should allow for stress relief by lateral expansion in regions "A" and "B" leading to a mismatch dislocation developing during the energy minimization process.

We then performed different energy minimization calculations with varying numbers of layers and varying concentration in regions "A," "B," and "C." The depth of the gap was changed accordingly in regions "A" and "B." This process therefore allowed us to change the depth of the dislocation core.

The resulting surface topography of the calculated crystal was then compared with STM line scans to determine the correlation between both data. All results were similar to Fig. 1(b) invariably showing a splitting into two partial dislocations, forming two shallow ditches on the surface, a phenomenon not observed with STM. These measurements only showed single ditches for these dislocation systems. The result of the calculations showed almost no dependence on variations of the concentration profile while the depth of the dislocation core is influenced by the depth to which atoms have been removed in the initial configuration.

Dissociation of a perfect dislocation $\mathbf{b}_1$ into partials $\mathbf{b}_2 + \mathbf{b}_3$, according to Frank's criterion,[27] can occur if $b_1^2 > b_2^2 + b_3^2$, which is true for our configuration. The distance between the two dislocation cores depends on two counteracting forces: a repelling force between them varying with $1/r$, r being the separation of the partials and an attracting force depending on the stacking fault energy.[27] We therefore conclude that the large separation of the partials is due to the fact that the stacking fault energies described by the EAM are too low. To verify this assumption, we have calculated the (intrinsic) stacking fault energy for pure nickel and found a value of 0.54 meV/Å^2, one order of magnitude too small compared with the experimental value of 5 meV/Å^2.[28] This fact accounts for a separation too large compared with STM measurements.

B. Inclined stacking fault configuration on a $Pt_{25}Ni_{75}(111)$ surface

For this type of calculation, we have modeled the dislocation system marked "C" in Refs. 1 and 2. Figure 2 shows a schematic drawing of this type of dislocation system with the region that we used for our calculations. We call this ensemble "inclined stacking fault configuration" because the $(1\bar{1}\bar{1})$ intrinsic stacking fault plane is inclined at an angle of 70.5° to the surface. The dislocation in this system has a Burgers vector of $\frac{1}{3}[1\bar{1}\bar{1}]$. One of the pronounced features of this dislocation system is the formation of a step at the surface with a height of 1/3 of a monatomic step.

Based on the information of the average concentration of the Pt enriched layer obtained by STM and recent ion scattering spectroscopy (ISS) measurements[29] we generated crystals in the same manner as described previously, but with the longer axis in the $[2\bar{1}\bar{1}]$ direction, perpendicular to the dislocation line. The slab was 6 nm thick

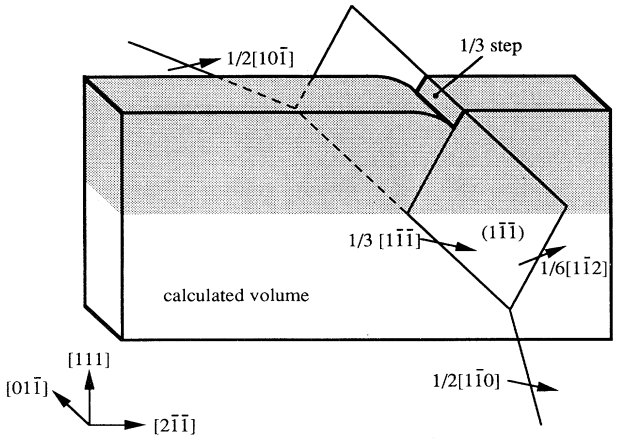

FIG. 2. Schematic drawing of the "inclined stacking fault configuration." The box-shaped volume represents the calculated geometry. This is a detail of the subsurface dislocation network depicted in Refs. 1 and 2. The picture shows two partial dislocations reaching the surface, corresponding to dislocation system "C" in this reference. The (1$\bar{1}\bar{1}$) plane in the figure represents an intrinsic stacking fault. The arrows represent the Burgers vector of the dislocation lines and the shaded area represents the part of the configuration with enriched Pt concentration due to preferential sputtering.

(30 monolayers) and the surface area was 6.7 nm × 1.3 nm (150 atoms/layer). To allow for the intrinsic stacking fault to develop in the course of the simulations, we removed rows of atoms in the (1$\bar{1}\bar{1}$) plane down to a certain depth into the crystal. The atoms of the two neighboring (1$\bar{1}\bar{1}$) planes were moved towards the center of the slot so as to form a more realistic starting point for the calculations and form equidistant gaps between the moved (1$\bar{1}\bar{1}$) planes [see Fig. 3(a)]. Periodic boundary conditions have been applied in the [2$\bar{1}\bar{1}$] and [01$\bar{1}$] directions to form the slab geometry. Again, the different atomic species were distributed randomly in each layer.

For the simulations we used two different sets of Pt concentration in regions "A" and "B" (50% Pt in region "A" and 37.75% Pt in region "B" for the first set and 43.75% Pt in region "A" and 34.375% Pt in region "B" for the second set). Region "C" was always kept at bulk composition (25% Pt). For both sets we then varied the number of layers in region "A" from 0 to 4 layers and in region "B" from 1 to 8 layers. This also meant that the depth of the slot had to be changed accordingly. The slot always spanned across regions "A" and "B."

In order to compare the results with STM line scans, we averaged over the positions of the atoms in the [01$\bar{1}$] direction and compared the depth profile of the first monolayer with STM line scans across the dislocation.

The EAM results show that a pronounced 1/3 monatomic step at the intersection of the stacking fault plane with the surface is formed only if the dislocation core is relatively deep inside the crystal (8 layers or more from the surface). Only minimal surface effects occur if the dislocation core is near the surface. This effect does not depend on variations of other simulation parameters (concentration profile, initial atom positions), therefore the comparison of the STM line scans with computed surface topography as described above can be used for determining the depth of the dislocation core. For the determination of the concentration profile it turned out that a variation of the Pt concentrations in the different layers only caused minor changes of the surface topography.

Comparing our results with STM measurements for the Ar sputtered alloy, we found the best agreement of ex-

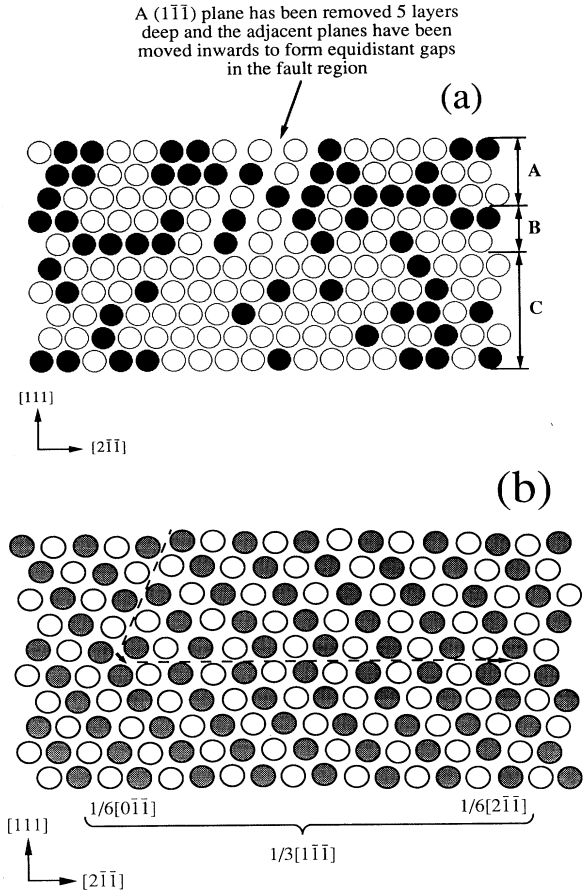

FIG. 3. Side view of the "inclined stacking fault configuration" used as input (a) for the calculation of the dislocation system "C" in Refs. 1 and 2 and the calculated configuration (b) (only the region in the vicinity of the dislocation core is shown). Region "A" is three layers thick and has 50% Pt concentration, region "B" is two layers thick and has a concentration of 37.5% Pt. Region "C" (the bulk) actually is 25 layers thick and has a concentration of 25% Pt. In (a), dark circles represent Pt atoms, light ones Ni. A (1$\bar{1}\bar{1}$) plane has been removed in regions "A" and "B" and the adjacent planes have been moved inwards. In (b), different planes in the [01$\bar{1}$] direction were marked by white and grey circles for improved visibility. The dislocation cores are marked by arrows, indicating the corresponding Burgers vectors whose values are given below. The step height where the dislocation reaches the surface is 1/3 of the interlayer distance.

perimental and calculational data for the configuration where region "A" consisted of 3 layers 50% Pt, region "B" of 2 layers 37.5% Pt, and region "C" of 25% Pt (Fig. 4). This concentration profile is in rough agreement with ISS measurements indicating 43% Pt (Ref. 30) and Auger data indicating 46% Pt (Ref. 2) on the surface. The results obtained showed good agreement with STM line scans. Therefore we conclude that the dislocation core (Burgers vector $\frac{1}{3}[1\bar{1}\bar{1}]$) was 5 layers below the surface for an alloy sputtered with 500 eV Ar at a flat angle of incidence (70° to the surface normal). We found that this dislocation core splits into two partials with Burgers vectors $\frac{1}{6}[0\bar{1}\bar{1}]$ and $\frac{1}{6}[2\bar{1}\bar{1}]$. Both dislocation lines are approximately six lattice constants apart from each other (see Fig. 3), depending slightly on the concentration profile. Although this spacing is too large and therefore leads to the formation of a small ditch directly above the $\frac{1}{6}[2\bar{1}\bar{1}]$ dislocation not observed by STM (due to an incorrect stacking fault energy produced by the EAM functions as described previously), the result nevertheless shows the formation of the 1/3 monatomic step exactly as observed with the STM.

Sample cleaning for the STM measurements has also been performed by Xe sputtering under the same sputtering conditions. The correspondence between STM line scans and computed data was not as perfect as for the Ar sputtered alloy, nevertheless we could show that the dislocation core is ≈2–4 layers below the surface. The fact that the location of the dislocation core is not as deep for the Xe sputtered alloy as for the one sputtered with Ar is due to the smaller penetration depth of the (larger) Xe atoms. Therefore the intermixing of the alloy constituents is less extensive in this case, leading to smaller numbers of Pt enriched layers.[1,2]

With the process described above, this type of calculation can provide valuable data that can hardly be derived from surface analysis techniques, e.g., the exact depth of the dislocation cores and thereby the number of Pt enriched layers. Depth profiling by sputtering cannot be used since it intermixes the components of the alloys. Possible methods where information about the concentrations of deeper layers can be obtained are angle resolved photoelectron spectroscopy and angle resolved Auger electron spectroscopy which suffer from diffraction

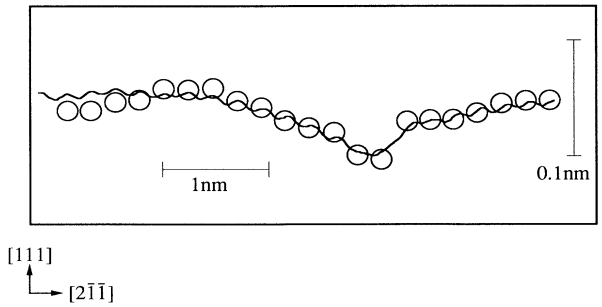

FIG. 4. STM line scan (averaged) of an Ar sputtered alloy superimposed on the averaged topography of the first monolayer of the calculated inclined stacking fault configuration (circles). The same input data as in Fig. 3 were used.

effects on single crystals, however. Therefore the type of calculations we performed offers a new method of obtaining data for deeper layers which are not easily available by other experimental methods.

C. Calculation of the dislocations on a $Pt_{10}Ni_{90}(110)$ surface

In our simulations of dislocations on a $Pt_{10}Ni_{90}(110)$ surface we made an equivalent approach to the one we used for the $Pt_{25}Ni_{75}(111)$ crystal. We used a similar concentration profile since the Pt enrichment due to preferential sputtering on this surface is equivalent to the one found for the $Pt_{25}Ni_{75}(111)$ crystal. Therefore the crystal was divided into three regions [marked "A," "B," and "C" in Fig. 5(a)] with different Pt concentrations. Two $(1\bar{1}0)$ planes have been removed in regions "A" and "B" and the adjacent planes were moved inwards to form equidistant gaps in the fault region. This should allow for a perfect dislocation to develop in the course of the calculations. The crystal was 10.2 nm × 1.4 nm at the surface and 6.2 nm thick (50 layers). Periodic boundary conditions have been applied in the directions parallel to the surface, thus forming a slab geometry. The bulk concentration (region "C") is 10% Pt, region "A" was assumed with 25% Pt, and region "B" with 20% Pt. For the simulations we varied the thickness of regions "A" and "B" between two and eight layers.

By watching whether a dislocation climbs during the energy minimization process (indicating an unstable configuration) it is possible to roughly determine the stability of a dislocation. Thereby we note that a configuration becomes more stable if the Pt enriched layer is thicker and the dislocation core is deeper below the surface. Moreover, dislocations are most stable if the dislocation core is approximately in the same depth as the interface between the Pt enriched region and the bulk. From previous results of the $Pt_{25}Ni_{75}(111)$ crystal it was determined that the thickness of the Pt enriched region is approximately five layers (≈ 10.5 Å) when sputtered with 500 eV Ar^+ ions at flat incidence. Since TRIDYN[31] simulations showed only minor differences of the penetration depths between $Pt_{25}Ni_{75}$ and $Pt_{10}Ni_{90}$ alloys, the thickness of the Pt enriched layer should be roughly the same for both crystals. Due to the smaller interlayer distance of the (110) crystal, the Pt enriched region is approximately eight layers thick on the $Pt_{10}Ni_{90}(110)$ crystal.[3] For comparison with experiment we used the simulations where both regions "A" and "B" were four layers thick each.

By analyzing the elastic energies of various configurations it was found that in some configurations the dislocations reduce their energy by forming jogs, i.e., short pieces going up and down along the [112] and $[\bar{1}\bar{1}2]$ direction instead of following straight along the [001] direction. Additionally, the $\frac{1}{2}[1\bar{1}0]$ perfect dislocation here splits into two Shockley partials $\frac{1}{6}[2\bar{1}1]$ and $\frac{1}{6}[1\bar{2}\bar{1}]$. A comparison of the energies showed that the elastic energy is reduced by 0.4 eV/nm in the [001] direction when the perfect dislocation splits up into Shockley partials. For calculating these dislocations, we moved atoms from

below the dislocation line to a position above it in the initial configuration.

Figure 5 shows different $\frac{1}{2}[1\bar{1}0]$ dislocation lines with its core eight layers deep. The pictures on the right show cross sections through the dislocation cores. Figure 5(c) shows the configuration where the perfect dislocation splits into Shockley partials. The width of the ditch formed thereby was ≈60–90 Å in the experiment and ≈50–55 Å in the simulation. The depth was ≈ 0.3 – 0.5 Å in the STM measurements and ≈0.6 Å in the calculations. This good agreement reflects the fact that there is no glide plane parallel to a (110) plane [in contrast to the (111) surface] and therefore an extended splitting of the dislocations such as below the (111) surface is impossible on the (110) face.

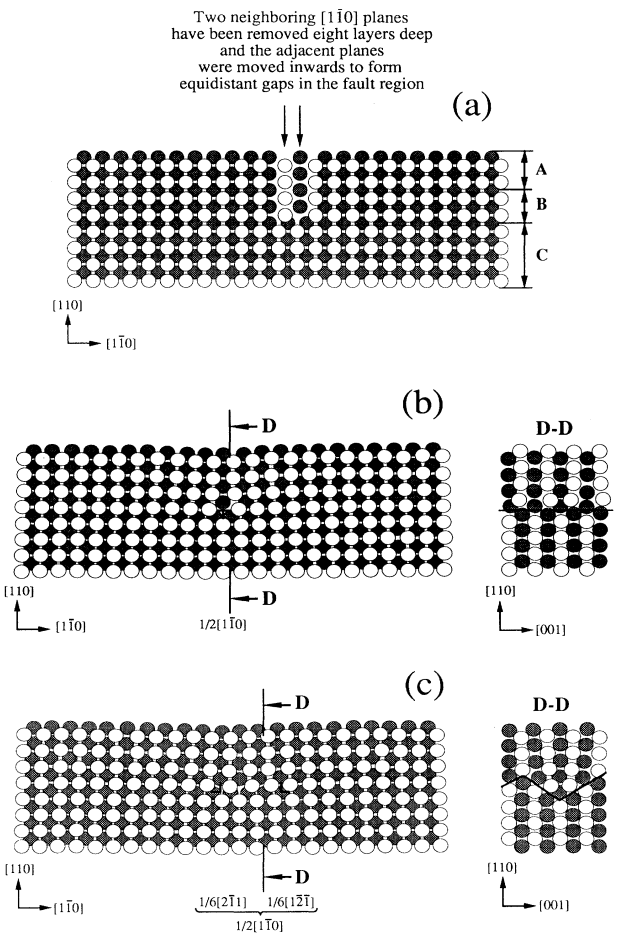

FIG. 5. Simulation of a mismatch dislocation below a $Pt_{25}Ni_{75}(110)$ surface. (a) Input crystal used for the energy minimization calculations. This is a detail of the actual crystal showing the area where atoms have been removed to allow for the dislocations to develop. Layers "*A*" contain 25% Pt, layers "*B*" 20% Pt, and layers "*C*" (bulk) 10% Pt. (b) Cross sections perpendicular and parallel to the dislocation line of the simulation result using configuration (a) as input. The left picture shows the dislocation core marked by the "*T*" symbol, the picture on the right shows a cross section along "*D-D*." (c) Cross sections perpendicular and parallel to the dislocation line of the simulation results using an input configuration similar to (a), but with one atom moved from below the dislocation line to a position above it. The graph on the left shows two dislocation cores of the Shockley partials (inverted "*L*" symbols), the graph on the right a cross section along "*D-D*." The partial dislocation lines run along the [112] and [$\bar{1}\bar{1}$2] directions, spanning stacking faults in the ($\bar{1}\bar{1}$1) and (111) planes, respectively.

It is interesting to note that for the (111) surface, all configurations with a Pt enriched region thicker than 4.2 Å (two monolayers) were stable while for the (110) surface this holds true only when the dislocation core is below a critical depth of approximately six layers (7.5 Å). This reflects the fact that (111) planes are nearly perfect glide planes as concluded from experimental evidence.[2] On the (110) surface, experiments have shown a pronounced dependence of dislocation density (and hence of their stability) on the thickness of the Pt enriched layer.[3]

IV. CALCULATION OF SURFACE CHEMICAL ORDERING

Apart from the dislocation phenomena discussed in the preceding section, surface short-range ordering was observed by STM under certain tip conditions on the $Pt_{25}Ni_{75}(111)$ crystal. We investigated this phenomenon using Monte Carlo calculations, where the ordering pattern developed itself during the calculations.

For the simulations we used a configuration where the surface was 3.6 nm×6.4 nm and the thickness 2.2 nm, containing 384 atoms in each layer, 4224 overall. Periodic boundary conditions have been applied in the direction perpendicular to the surface. In this manner a slab geometry was formed (eleven layers thick).

The bulk concentration range was varied from 35% Pt to 40% Pt. Although this is quite different from the actual bulk concentration, we have chosen these values for the following reason: The Monte Carlo approach can only simulate thermodynamic equilibrium. Experimentally, a region at the surface with a kind of local thermodynamic equilibrium different from the bulk was found.[3,29,32] This is due to the fact that the annealing temperature in the experiments is too low to allow diffusion between the bulk and the surface layers (which are Pt enriched due to preferential sputtering). At the annealing temperature used in the experiment, diffusion can only occur within these surface layers. Mobilities are much higher at the surface, so that local equilibrium is reached there at much lower temperatures. For these reasons, using 25% Pt bulk concentration would lead to a surface concentration of approximately 35%–40%, obviously much too low compared with low energy ion scattering spectroscopy data indicating 45%–55% Pt at the surface. Therefore and due to the pronounced Pt enrichment due to preferential sputtering 35%–40% Pt substrate concentration is a good representation of the conditions in the subsurface layers, although the actual bulk concentration is only 25% Pt.

Calculations with Pt concentrations larger than 40% could not be performed since from that concentration on until about 75% Pt the bulk forms a tetragonal $L1_0$

phase.[14] Although this is correct for a 50% Pt alloy, the tendency of forming such a phase is a bit too pronounced with the functions we used here, compared with the Pt-Ni phase diagram.[22] Therefore we did not extend the Pt concentration range beyond 40% Pt. The results, however, show that the best match between calculated and measured ordering pattern is below 40% Pt concentration.

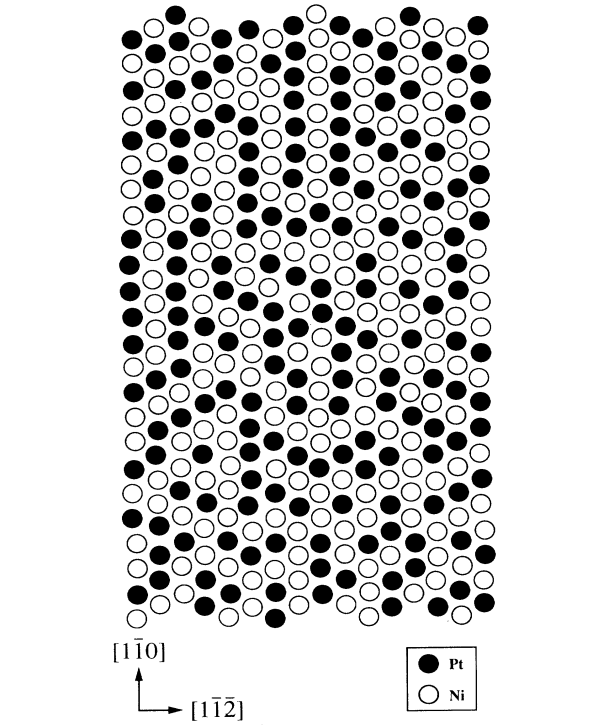

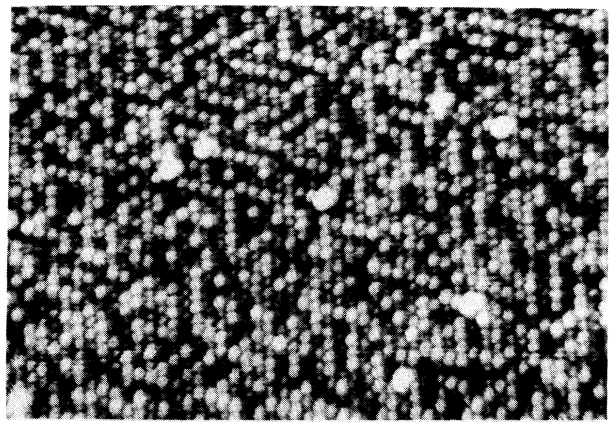

FIG. 6. Atomic arrangement on the (111) surface of a PtNi single crystal calculated by Monte Carlo simulations and the corresponding STM image. Bulk composition for the calculations was 38% Pt and 62% Ni; the temperature was 420 K. The agreement between the calculated pattern and the STM image of a $Pt_{25}Ni_{75}$ single crystal is obvious: both images show short rows of up to seven atoms of the same atomic species. In both images there are also some triangular structures visible, made up of these rows inclined at an angle of 60°. The large bright spots on the STM image are supposed to be impurities.

The different ensembles were calculated at temperatures of 300 K, 500 K, 700 K, 900 K, and 1100 K. The results of these calculations showed a good agreement between the calculated and measured ordering patterns at the surface only for the bulk concentration range from 36% Pt to 38% Pt and the temperature range from 300 K to 500 K, although some short-range ordering was observed in all calculations.

The ordering observed on this surface shows some similarities to the (111) surface of the $L1_0$ structure. The phase diagram[22] shows that $Pt_{50}Ni_{50}$ forms an $L1_0$ structure below 930 K, consisting of alternating (001) planes of Pt and Ni, visible as parallel rows of alternating Pt and Ni in the [$\bar{1}$10] direction on a (111) surface. Due to the type of surface short-range ordering observed here, with three rotational domains, determination of a classical order parameter is not very helpful. We therefore use the length of the Pt or Ni rows as a rough indication of the degree of ordering. Since our surface layer concentration is 47% Pt in the simulations, the ordering is expected to be very close to the one for 50% Pt. This is the reason why we observe long rows of up to seven atoms in the simulations, matching the STM data.

Best agreement was found for $Pt_{38}Ni_{62}$(111) at 420 K. This temperature is much lower than the annealing temperature in the experiment (780 K), but we should note that cooldown was rather slow (approximately 10 min from 780 K to 400 K). Due to the high surface mobility, the sample may have had ample time to form a local equilibrium at the surface during cooldown. We therefore interpret the ordering pattern as a representation of the configuration frozen at a temperature of approximately 420 K. This result is shown in Fig. 6.

V. SUMMARY

We have performed energy minimization calculations for dislocation systems on $Pt_{25}Ni_{75}$(111) and $Pt_{10}Ni_{90}$(110) surfaces as well as Monte Carlo simulations for the $Pt_{25}Ni_{75}$(111) surface. The simulations of perfect dislocations on the $Pt_{25}Ni_{75}$(111) surface showed a splitting into two partial dislocations not observed by the experiment which we attributed to the fact that the (intrinsic) stacking fault energy is too low with the embedding functions we used. Calculations of stacking fault planes in the same crystal, inclined at the surface, with dislocations reaching the surface ("inclined stacking fault configuration") showed good agreement with STM measurements. The results for $Pt_{10}Ni_{90}$(110) show that there is a ditch formed above the dislocation core whose calculated depth and width again are in accordance with STM data. Finally, we calculated ordering phenomena on a $Pt_{25}Ni_{75}$(111) surface showing the same ordering pattern as observed with STM. From the simulation of dislocation phenomena we were able to determine the exact depth of the dislocation cores, adding valuable information that could not be obtained by experimental methods.

ACKNOWLEDGMENTS

This work has been supported by the Austrian Fonds zur Förderung der wissenschaftlichen Forschung, Projekt Nr. P8147-TEC. The authors are very grateful to Stephen Foiles (Sandia National Laboratories, Livermore) for supplying us with the computer code and for his substantial help in implementing the embedded-atom method.

[1] M. Schmid, A. Biedermann, H. Stadler, and P. Varga, Phys. Rev. Lett. **69**, 925 (1992).
[2] M. Schmid, A. Biedermann, H. Stadler, C. Slama, and P. Varga, Appl. Phys. A **55**, 468 (1992).
[3] M. Schmid, A. Biedermann, C. Slama, H. Stadler, P. Weigand, and P. Varga, Nucl. Instrum. Methods Phys. Res., Sect. B **82**, 259 (1993).
[4] Y. Gauthier, R. Baudoing, Y. Joli, J. Rundgren, J. C. Bertolini, and J. Massardier, Surf. Sci. **162**, 342 (1985).
[5] J. C. Bertolini, J. Massardier, P. Delichere, B. Tardy, B. Imelik, Y. Jugnet, Tranh Minh Duc, L. de Temmerman, C. Creemers, H. van Hove, and A. Neyens, Surf. Sci. **119**, 95 (1982).
[6] P. Weigand, P. Novacek, G. van Husen, T. Neidhart, and P. Varga, Surf. Sci. **269/270**, 1129 (1991).
[7] M. Schmid, H. Stadler, and P. Varga, Phys. Rev. Lett. **70**, 1441 (1993).
[8] M. S. Daw and M. I. Baskes, Phys. Rev. Lett. **50**, 1285 (1983).
[9] M. S. Daw and M. I. Baskes, Phys. Rev. B **29**, 6443 (1984).
[10] S. M. Foiles, Phys. Rev. B **32**, 7685 (1985).
[11] S. M. Foiles, in *Surface Segregation Phenomena*, edited by P. A. Dowben and A. Miller (CRC, Boca Raton, 1990), p. 79.
[12] M. Lundberg, Phys. Rev. B **36**, 4692 (1987).
[13] S. M. Foiles, Phys. Rev. B **40**, 11 502 (1989).
[14] H. Stadler, W. Hofer, M. Schmid, and P. Varga, Surf. Sci. **287/288**, 366 (1993).
[15] S. M. Foiles, M. I. Baskes, and M. S. Daw, Phys. Rev. B **33**, 7983 (1986).
[16] Ning Ting, Yu Qingliang, and Ye Yiying, Surf. Sci. Lett. **206**, L857 (1988).
[17] S. M. Foiles, Surf. Sci. Lett. **191**, L779 (1987).
[18] A. F. Wright, M. S. Daw, and C. Y. Young, Phys. Rev. B **42**, 9409 (1990).
[19] E. Clementi and C. Roetti, *Atomic Data and Nuclear Data Tables* (Academic, New York, 1974), Vol. 14, Nos. 3 and 4.
[20] A. D. McLean and R. S. Mc Lean, *Atomic Data and Nuclear Data Tables* (Academic, New York, 1981), Vol. 26, Nos. 3 and 4.
[21] A. F. Voter, S. P. Chen, R. C. Albert, A. M. Boring, and P. J. Hay, in *Atomistic Simulation of Materials—Beyond Pair Potentials*, edited by V. Vitek and D. J. Srolovitz (Plenum, New York, 1989), p. 223.
[22] C. E. Dahmani, M. C. Cadevilee, J. M. Sanchez, and J. L. Morán-López, Phys. Rev. Lett. **55**, 1208 (1985).
[23] R. Hultgren, P. D. Desay, D. T. Hawkins, M. Gleiser, and K. K. Kelly, *Selected Values of the Thermodynamic Properties of Binary Alloys* (American Society for Metals, Metals Park, OH, 1973).
[24] J. H. Rose, J. R. Smith, F. Guinea, and J. Ferrante, Phys. Rev. B **29**, 2963 (1984).
[25] J. E. Sinclair and R. Fletcher, J. Phys. C **7**, 864 (1972).
[26] See, for example, D. A. McQuarrie, *Statistical Mechanics* (Harper & Row, New York, 1976).
[27] J. P. Hirth and J. Lothe, *Theory of Dislocations, Second Edition* (Krieger, Malabar, FL, 1992).
[28] M. N. Shetty and K. Laha, Z. Metallkunde **77**, 397 (1986).
[29] P. Weigand, C. Nagl, M. Schmid, and P. Varga, Fresenius J. Anal. Chem. **346**, 281 (1993).
[30] P. Weigand, P. Novacek, G. van Husen, T. Neidhart, L. Z. Mezey, W. Hofer, and P. Varga, Nucl. Instrum. Methods Phys. Res., Sec. B **64**, 93 (1992).
[31] W. Möller and W. Eckstein, Nucl. Instrum. Methods B **2**, 814 (1984).
[32] P. Weigand, W. Hofer, and P. Varga, Surf. Sci. **287/288**, 350 (1993).

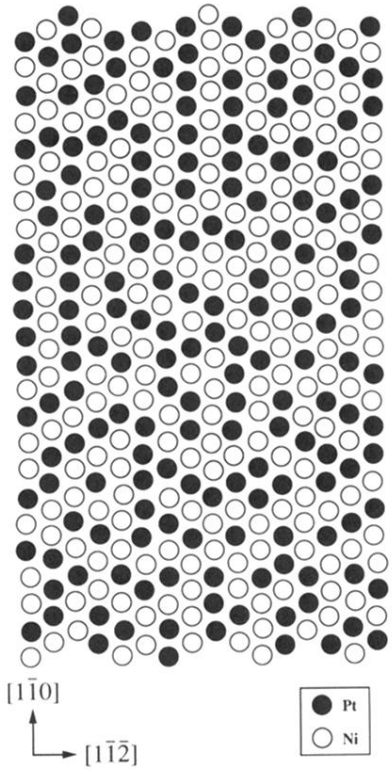

FIG. 6. Atomic arrangement on the (111) surface of a PtNi single crystal calculated by Monte Carlo simulations and the corresponding STM image. Bulk composition for the calculations was 38% Pt and 62% Ni; the temperature was 420 K. The agreement between the calculated pattern and the STM image of a $Pt_{25}Ni_{75}$ single crystal is obvious: both images show short rows of up to seven atoms of the same atomic species. In both images there are also some triangular structures visible, made up of these rows inclined at an angle of 60°. The large bright spots on the STM image are supposed to be impurities.